A Metallic Additively Manufactured Metamaterial for Enhanced Monitoring of Acoustic Cavitation-Based Therapeutic Ultrasound

Luzhen Nie, David A. Hutchins, Lorenzo Astolfi, Timothy P. Cooper, Adam T. Clare, Chris Adams, Richard L. Watson, Peter J. Thomas, David M. J. Cowell, James R. McLaughlan, Stefano Laureti, Marco Ricci, and Steven Freear*

The combination of ultrasound and microbubbles allows treatment of indications that would be impossible or too risk adverse with conventional surgery. During treatment, subharmonic and ultraharmonic components that can only be generated from microbubbles are of great interest for intraoperative monitoring. However, the microbubble emissions are several orders of magnitude lower in power compared to that of the fundamental frequency component from the ultrasound applicator, resulting in a low signal-to-noise ratio (SNR) for monitoring. A 3D acoustic metamaterial (AMM) immersed in water is proposed for suppressing unwanted ultrasound waves, which allows the improved sensitivity for detecting weak microbubble emissions. Numerically, the importance of shear waves on the AMM transfer properties is highlighted, though only longitudinal ultrasound waves are transmitted through water. Experimentally, the design is implemented in titanium using additive manufacturing, with an attenuation level of 40 dB at the fundamental frequency. Consequently, the application of the AMM efficiently improves the SNR for subharmonic and ultraharmonic microbubble emissions by 11.8 and 11.9 dB, respectively. The subharmonic components originally overwhelmed by noise are recovered. This is the first time that AMMs have been applied to passive acoustic monitoring and this work stands to improve treatment outcomes from cavitation-mediated focused ultrasound therapy.

1. Introduction

There is significant interest in using ultrasound for noninvasive therapy both in the laboratory and clinically.[1] The aims of therapeutic ultrasound are varied, encompassing killing of cancerous cells[2] and opening of the biological membrane for enhanced drug uptake.[3–6] Acoustic cavitation refers to the formation and/or activity of gaseous cavities (microbubbles) driven by acoustic radiation,[7] and acoustic cavitation-based procedures achieve therapeutic benefits by harnessing the corresponding microbubble activity.[8,9] There is significant research enthusiasm in using cavitation-based procedures for noninvasive treatment of neurological indications.[3] These procedures prevail in treating a wide range of locations within the brain without overheating the skull. During treatment, microbubbles volumetrically pulsate when subject to an ultrasonic field, and their response can be classified in two types: "noninertial" (stable) and "inertial" (transient) cavitation.[10] Generally, for low- and mid-level pressure amplitudes, stable microbubble oscillations about its equilibrium

---

L. Nie, D. M. J. Cowell, J. R. McLaughlan, S. Freear
School of Electronic and Electrical Engineering
University of Leeds
Leeds, LS2 9JT, UK
E-mail: s.freear@leeds.ac.uk

D. A. Hutchins, L. Astolfi, R. L. Watson, P. J. Thomas
School of Engineering
University of Warwick
Coventry, CV4 7AL, UK

The ORCID identification number(s) for the author(s) of this article can be found under https://doi.org/10.1002/adem.202100972.

T. P. Cooper, A. T. Clare
Department of Mechanical, Material and Manufacturing Engineering
University of Nottingham
University Park, Nottingham, NG7 2RD, UK

C. Adams
Physical Sciences Platform
Sunnybrook Research Institute
Toronto, ON, M4N 3M5, Canada

S. Laureti, M. Ricci
Department of Informatics, Modelling, Electronics and System Engineering
University of Calabria
87036 Rende, Italy

size can be sustained for many cycles. Fluid microstreaming is generated and exerts shear forces on surrounding cells to reversibly permeabilize their membranes for localized drug delivery.[11] At high-pressure amplitudes, inertial cavitation occurs with rapid growth and sudden collapse of the microbubble. High-amplitude shock waves which can mechanically damage nearby cells are emitted, and microjets can be potentially created to penetrate tissue.[11] To minimize undesired tissue damage especially in critical organs such as the brain and assess the treatment efficacy, the provision of reliable methods for real-time monitoring of these therapeutic procedures is necessary.

Passive listening to the acoustic emissions from the microbubbles under ultrasound exposures is of great interest in the context of uncovering the underlying microbubble dynamics and bioeffects for online monitoring and prediction of the therapeutic outcome.[12–17] Due to nonlinear microbubble oscillations, emissions at the subharmonic ($f_0/2$), ultraharmonic ($3f_0/2$) and integer harmonics (nf_0) of the drive frequency (f_0) are generated. Relating the subharmonic[18] and ultraharmonic acoustic emissions[13] to cavitation activity constitutes a beneficial solution as they only arise from microbubbles. However, the detection of both the subharmonic and ultraharmonic with high sensitivity represents a challenge. This is because the received signal is dominated by the fundamental frequency component from the ultrasound applicator, whose power can be a few orders of magnitude higher than the subharmonic and ultraharmonic. To avoid saturation in acquisition, weak harmonic signatures of cavitation thus only utilize a small portion of the dynamic range of the analog-to-digital converter (ADC), and their detection is detrimentally affected by quantization errors.[19] Analog filters consisting of resistors, capacitors, inductors, and operational amplifiers could be placed before the ADC to attenuate the fundamental frequency component in the analog domain.[20] This allows the subharmonic and ultraharmonic to efficiently make use of the ADC dynamic range, leading to high-fidelity detection of these weak cavitation features. However, implementing or modifying analog hardware filters can be difficult once the ultrasound system is built as the access to its analog front-end is usually constrained.[21] This fact thus warrants the design of filtering devices to suppress ultrasound waves as they propagate and before being captured by any electronic device or detector.

To tackle this problem, this work uses acoustic metamaterials (AMMs) which are artificially architected structures designed to control acoustic wave propagation.[22] AMMs possess a number of extraordinary properties such as negative refraction and nonreciprocal wave transmission that are not encountered for natural materials.[23] Widespread interest has been seen in the development of AMMs with spectral bandgaps, where a range of frequencies exist over which the propagation of acoustic waves through the material is suppressed.[24] The motivation for studying this type of AMM is driven by diverse potential applications. Examples include acoustic wave abatement,[25] filtering,[26] and guiding.[27] In AMMs, the propagation of acoustic waves is affected by both the geometry of the structure, i.e., meta-atoms or also referred as unit cells, and the properties of the constituent materials. A wide range of metamaterials have been identified that can result in bandgaps by modifying a base material to contain meta-atoms such as scattering units[24] and/or local resonators.[28] When scattering units are arranged periodically in a base material with the unit size and lattice constant on the same order of the acoustic wavelength, Bragg bandgaps can be formed due to destructive interference of the waves scattered from neighboring inclusions.[24] In this case, the operation frequency is primarily determined by the characteristic dimensions of the scattering unit. Though typically unit cells embedded with local resonators are positioned periodically, resonance-mediated bandgaps do not rely solely on structural regularity. Structures with deep subwavelength resonators are able to attenuate the amplitude of the transmitted acoustic wave whose wavelength can be two orders of magnitude larger than the characteristic size of the resonating elements,[29] but the resonant AMMs operate over a narrow bandwidth.[25,29]

Efforts have been devoted to the creation of AMMs exhibiting wide bandgaps,[30–33] and these designs are generally adaptable to different applications by tuning the inclusion dimensions or changing the constituent materials. However, the complex geometries of these designs result in substantial fabrication challenges which are intractable by using conventional manufacturing methods such as computerized numerical control machining and laser cutting. Additionally, for these designs a large acoustic impedance mismatch between the base material and inclusions is essential to generate sufficient scattering and interference. Fortunately, recent additive manufacturing developments have facilitated the fabrication of many complex AMMs at different length scales and are still rapidly evolving.[25,34–36] Acoustic impedance is the product of the speed of sound and density of a given material.[37] For airborne applications, the mismatch in acoustic impedance between air and polymers or similar materials is large enough to achieve efficient scattering at their interface and form a wide bandgap.[31,32] However, this is not the case when the transmission medium is water for use in biomedical ultrasound,[1] and thus alternative materials and fabrication methods are needed.[38]

In the current study, an optimized metallic bandgap AMM is designed for a transmission medium of water, metals being chosen for the manufacture of the AMM as their values of acoustic impedance are typically much higher than those of polymers. Laser power bed fusion (LPBF) is capable of reproducibly manufacturing metallic structures with submillimeter accuracy,[35] and it was adopted to fabricate the AMMs. This accuracy would allow the built AMM to be employed for monitoring acoustic cavitation-based transcranial ultrasound therapy.[3] Scanning electron microscopy (SEM) was employed to visualize the details of the printed parts. Ultrasonic transmission measurements were then performed and compared with the numerical predictions. The application of the optimized AMM was finally shown to detect the acoustic emissions from an acoustic contrast agent (SonoVue, Bracco S.p.A, Milan, Italy).

2. Metamaterial Design and Numerical Simulations

The design of the AMM originated from a cubic unit cell consisting of spheres concentrated at each corner connected by cylindrical struts, with which wide bandgaps could be achieved.[32] As shown in **Figure 1**a, the unit cell is characterized

(a)

(b)
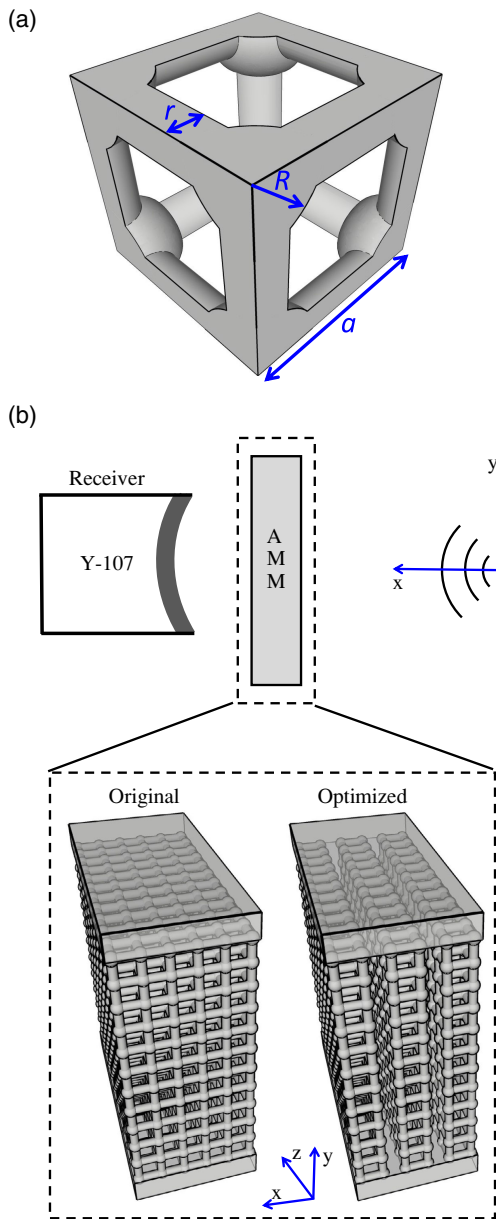
Figure 1. a) Schematic diagram of the unit cell and b) simulation setup. Inset in (b): illustration of AMMs with original and optimized designs composed of 5 continuous layers (x axis) and 3 separate layers, respectively.
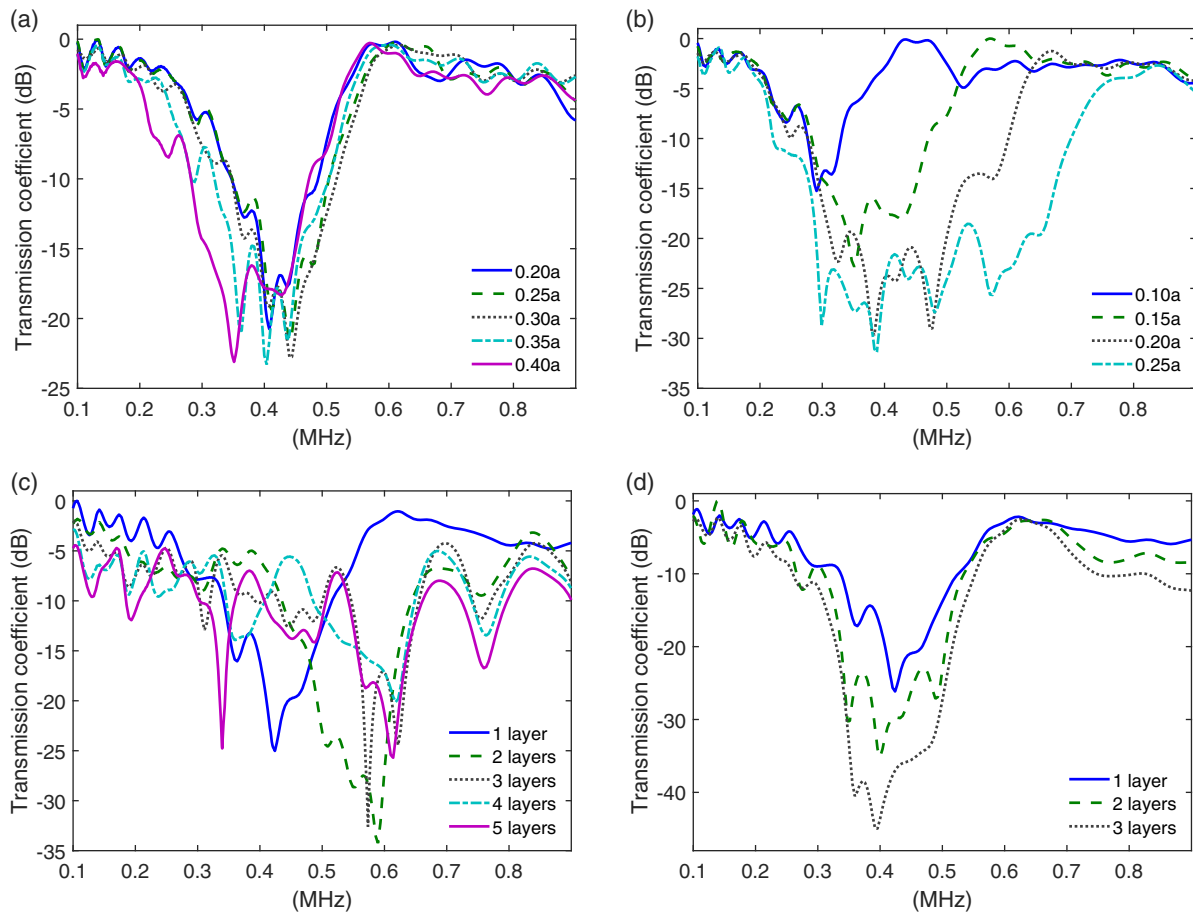
by the strut radius r, sphere radius R, and the lattice constant a. Additive manufacturing with titanium has been well established in LPBF, and it was selected as the AMM constituent material.

For both the simulations and experiments, the lattice constant a was 1.4 mm, a value with which the sample could be reproducibly fabricated by using the LPBF system in this study. To optimize the AMM design, 3D numerical simulations in the time domain were performed by using PZFlex (OnScale Inc., USA). This is a commercial finite element modeling package which has been successfully used for the development of a broad range of ultrasonic devices including AMMs.[35] In simulations, the acoustic properties of water were characterized by a

speed of sound of 1490 m s^{-1} and density of 1000 kg m^{-3}. For titanium, the speed of sound was 6100 m s^{-1}, the shear wave speed was 3100 m s^{-1}, and the density was 4480 kg m^{-3}. A cubic spatial grid was employed with a mesh size $\Delta x = \Delta y = \Delta z = 46\,\mu$m. A commercially available ultrasound transducer (Y-107, Sonic Concepts Inc., WA, USA) was modeled in this study and used in experiments. It had a large bandwidth of 10 kHz–15 MHz, an active diameter of 17.5 mm, and a spherical focal depth of 64 mm. The simulation setup is shown in Figure 1b. To model this transducer, a curved surface having the same geometry and centered about the x axis was created. The spherical focal point of the transducer was defined as the spatial origin. At the origin, a point source emitting spherical waves was simulated, for ease of modeling with the Y-107 transducer as the receiver. To achieve this, toward the Y-107 transducer a broadband plane wave packet with an amplitude of 100 kPa at each frequency was applied to a $184 \times 184\,\mu$m square region centered about the x axis. This approach of generating spherical waves is similar to that used in synthetic aperture ultrasound imaging.[39] For all designs, the AMM was placed symmetrically about the x axis, with a distance of 45 mm from the center of its incident face to the spatial origin. For each layer along the x axis, the unit cell was periodically repeated along both the y and z axes to build up samples always having 23×23 cells to fully cover the transducer. Absorbing boundaries were adopted to prevent undesired reflections, thus simulating anechoic conditions.

The effects of sphere and strut geometric features on the evolution of bandgaps were first numerically investigated with a single-layer (x axis) structure. The frequency dependence of the ultrasonic transmission coefficient was determined by calculating the ratio between the fast Fourier transform (FFT) amplitudes of the transmitted signals with and without the AMM. With a fixed strut radius r, the bandgap size gradually increases with an enlarged sphere radius R, as shown in **Figure 2**a. A pronounced impact from the strut size is seen on the formation of the bandgap as shown in Figure 2b. For a fixed sphere radius R, the bandgap significantly widens with an increased strut radius r.

Numerical simulations showed that the wavelengths that existed over the bandgap frequency range were of the same order of magnitude as the size of the lattice constant, and that the bandgap was shifted to a higher frequency with a smaller lattice constant. Given the lattice constant of 1.4 mm, a bandgap center frequency of 400 kHz was considered and it is a clinically relevant value.[3] The strut and sphere radii of 0.16a and 0.25a were chosen to operate selective frequency filtering at around 400 kHz while preserving its subharmonic (200 kHz) and ultraharmonic (600 kHz) components. For the primitive design similar to the cases in the literature,[31–33,40] the single-layer structure was periodically repeated along the x axis to form samples with 2, 3, 4, and 5 layers. The transmission coefficient curves for varied sample thicknesses are plotted in Figure 2c, and there are no stable and well-defined bandgaps when changing the number of sample layers, which differs from the case in air.[40] For bandgap-generating AMMs with a continuously periodic arrangement, a unit cell is usually applied with infinite periodicity as the outer boundary condition to predict the position and width of a bandgap.[32] However, the current result shows that these bandgap properties could be thickness dependent, suggesting

**ADVANCED
SCIENCE NEWS**

www.advancedsciencenews.com

**ADVANCED
ENGINEERING
MATERIALS**

www.aem-journal.com

Figure 2. Numerical simulations of the AMM transfer properties. a) The effect of the sphere radius R. b) The effect of the strut radius r. In (a), a single-layer (x axis) structure with a strut radius $r = 0.15a$ was investigated for $R = 0.20a$, $0.25a$, $0.30a$, $0.35a$, and $0.40a$. In (b), a single-layer (x axis) structure with a sphere radius $R = 0.40a$ was investigated for $r = 0.10a$, $0.15a$, $0.20a$, and $0.25a$. $a = 1.4$ mm. c) Influences of the sample thickness (x axis) for the continuous-layer arrangement. d) Transfer properties for the optimized design with separate layers where the struts linking neighboring layers (x axis) were removed. For (c) and (d), $R = 0.25a$, $r = 0.16a$, and $a = 1.4$mm.

the necessity of investigating the effect of the sample thickness when designing a practical structure composed of finite layers for use in water.

The conversions between longitudinal and shear waves can occur through reflection or refraction at the boundary between the solid inclusions and water.[41] This means that even if only longitudinal ultrasound waves are transmitted, shear waves can exist within the solid inclusions due to this mode conversion mechanism. (Note that water does not support shear wave transmission.) We propose that the remarkable phenomenon found in Figure 2c could be attributed to the wave mode conversions and coupling between longitudinal and shear waves through different layers. To verify this, the struts between each set of 3D layers (each aligned along the x axis) were modified by setting the shear wave speed to zero for the original design with up to 5 continuous layers. Under this setup, it was found that the dip in the transmission spectrum became wider and deeper for an increased sample thickness.

For a realistic design with the capability to operate controllable filtering over a bandwidth of interest, the solid struts combining adjacent 3D layers (x axis) were removed and replaced with water

to cut off shear wave propagation. The inset in Figure 1b schematically shows the optimized design of separate layers with its counterpart of continuous layers (i.e., with no water gap) for comparison. An outer solid wall covering the whole cross section was added to the structure to offer a flat surface for mounting it in experiments. In manufacturing, these walls had a thickness of 3 mm. For ease of visibility in Figure 1b, the top walls were made transparent and each layer was composed of 11×11 cells. Figure 2d shows the results for the optimized design made of separate layers. Compared with Figure 2c, the variation of the bandgap location was relatively small for changes in sample thickness, which is a desirable feature for selective filtering.

3. Experiments and Results

3.1. Additive Manufacturing

Experiments were needed to confirm the existence of the bandgaps in transmission observed in the numerical simulations, for both the 5-continuous-layer and 3-separate-layer structures

(Figure 1b). Hence, these two structures were additively manufactured. Note that these two designs had the same thickness. As simulated in Figure 2d, the optimized 3-separate-layer design provided about 43 dB of attenuation at 400 kHz with a sample thickness of about 2 wavelengths.

The metamaterial samples were manufactured by LPBF with a Renishaw AM125 system (Renishaw plc, New Mills, UK). The LPBF process made use of commercially available Ti–6Al–4V powder (15–45 µm, AP&C Powders), where a thin layer of the powder was deposited on a build platform, and a laser beam directed by a galvanometer scanned across the layer, melting the surface according to the CAD model sliced into layers. The platform lowered, the next powder layer was applied, and the process repeated to consolidate the fresh powder into the previous layer and build up the part. The build area was contained in a vacuum chamber, fed with inert gas.[42] The powder layer thickness was 30 µm, laser power was 100 W, hatch distance was 0.085 mm, and scanning speed was 928.6 mm s^{-1}. Finished parts were removed from the build platform by hand and supports required to prevent warping were cut and ground off using a Dremel rotary tool.

Figure 3a,b displays photographs of the fabricated samples, and Figure 3c shows an SEM image of structure details in the secondary electron mode. As shown in Figure 3c, the unit cell size of the printed structure agrees reasonably with the design, having a value of approximately 1.4 mm. The strut irregularity is more evident along the lateral direction (corresponding to the vertical orientation during LPBF), and the presence of spheres at the strut conjunctions is not so obvious. These could occur as a result of gravity that the melt powders drop before they set during manufacturing, locally enlarging the horizontal struts and resulting in structure modifications in comparison to the originally designed unit cells. The effects of altering the sphere radius could be small as illustrated in Figure 2a. The overall influences on the bandgap properties arising from the differences between the designed models and the manufactured ones have been investigated by ultrasonic transmission measurements in water, and they are discussed in the following section.

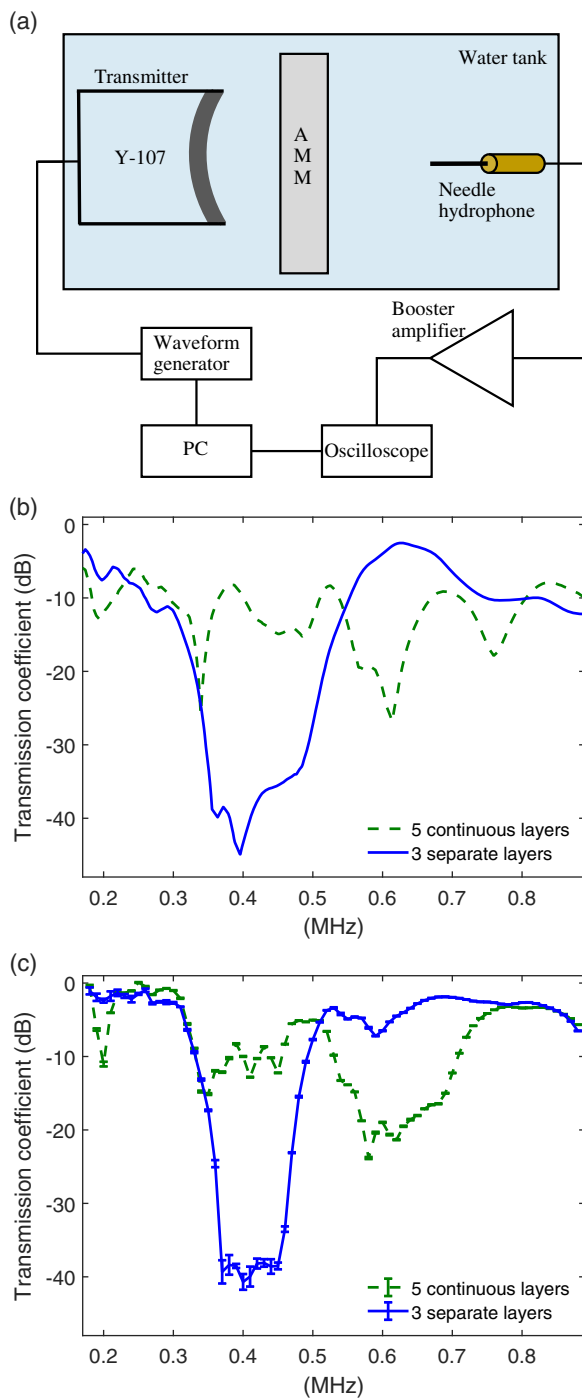### 3.2. Ultrasonic Transmission Measurements

Relying on the reciprocity property of acoustic wave propagation,[43] the transfer properties of the printed AMMs immersed in water were measured by using a Y-107 ultrasonic transducer as the transmitter and a 1 mm needle hydrophone (Precision Acoustics, Dorchester, UK) placed at the Y-107 focus as a point receiver. The experimental setup is illustrated in **Figure 4**a. Both the transmitter and receiver were immersed in water. The relative distance between the Y-107 transducer and the AMM was identical to that in the numerical simulations. Whenever an AMM was used in this study, after water immersion, the air bubbles still trapped in the AMM cavities were carefully removed by using water jets generated from a syringe.

The Y-107 transducer was driven by a waveform generator (33600A, Keysight Technologies, CA, USA) which supplied 20-cycle sinusoidal waveforms with a 10 V peak-to-peak amplitude, and the frequencies were swept from 180 to 880 kHz in increments of 10 kHz. The transmitted signal received by the needle

(a)

(b)

(c)
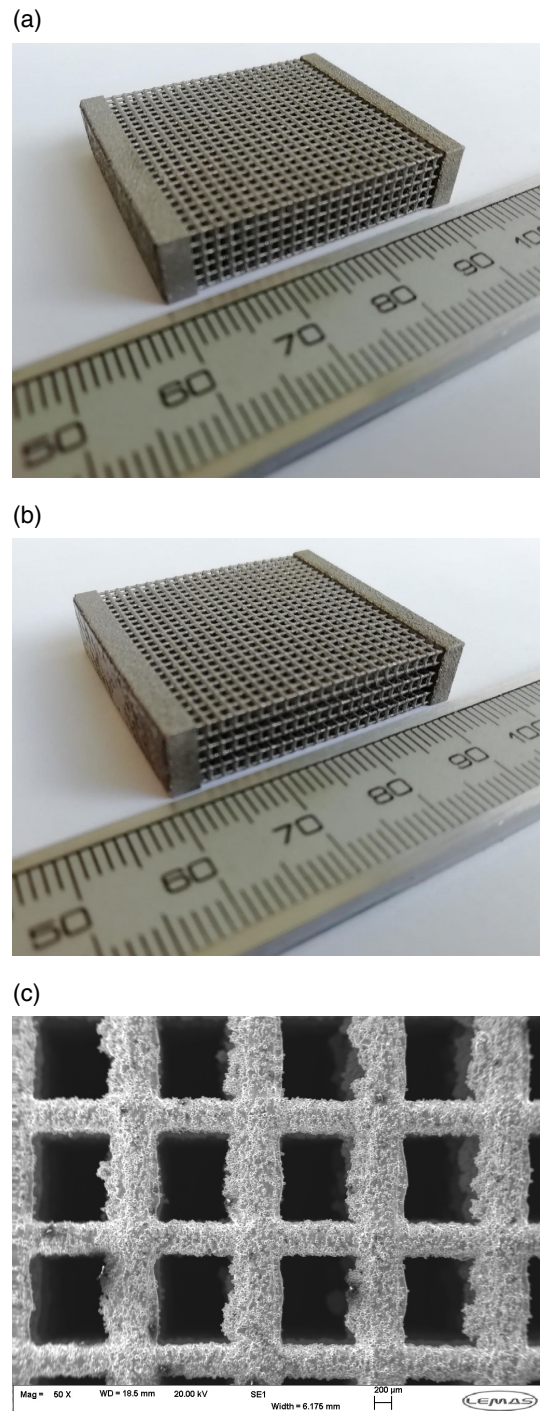
Figure 3. Additively manufactured samples. a,b) Photographs of the additively manufactured structures with the original and optimized unit cell arrangement, respectively. c) SEM image of the close-up view of structure details in the secondary electron mode.

hydrophone was amplified by a hydrophone booster amplifier (Precision Acoustics, Dorchester, UK) and then acquired by an MSO-S 104A oscilloscope (Keysight Technologies, Santa Rosa, USA) before removal to a local computer for postprocessing in MATLAB (Mathworks, MA, USA). The sampling frequency

**ADVANCED
SCIENCE NEWS**

www.advancedsciencenews.com

**ADVANCED
ENGINEERING
MATERIALS**

www.aem-journal.com

Figure 4. Comparisons between the numerical predictions and experimental measurements of the AMM transfer properties as a function of frequency. a) Schematic diagram of the experimental setup. b) Numerical predictions. c) Experimental measurements. For (b) and (c), the original and optimized designs consisted of 5 continuous layers (*x* axis) and 3 separate layers, respectively. The error bars in (c) show the standard deviations between five groups of measurements.

was set to 100 MHz. For each frequency, 500 measurements were averaged in one group, and in total five groups of measurements were taken for calculating the standard deviation.

Figure 4b,c shows the transmission coefficient as a function of frequency for both the original continuous-layer and optimized separate-layer structures. The numerical predictions are displayed in Figure 4b, and the experimental measurements are shown in Figure 4c. The calculation of the transmission coefficient for each frequency was conducted in an identical manner as outlined in the simulation section, and the reference signals were taken through water without the AMMs in place. It is evident that the numerical predictions and the experimental data are in reasonable agreement. The differences between Figure 4b,c could be due to manufacturing imperfections and differences between the assumed material properties in the simulations and the real ones in experiments. For the optimized design with 3 separate layers, a 40 dB transmission suppression at the designed operation frequency of 400 kHz is observable in Figure 4c. The unit cell deviations from the ideal geometry, as shown in Figure 3c, appear to be tolerable, as the location of the attenuation zone in the transmission spectrum matches well with the intended frequency. In contrast, for the original design deep dips in the transmission spectrum are also observable at both 200 and 600 kHz, the locations of the subharmonic and ultraharmonic components when manipulating microbubble activity with a fundamental frequency of 400 kHz. In addition, the amplitude suppression at 600 kHz is even stronger than that at 400 kHz (the frequency to filter out).

3.3. Use of the Optimized Metamaterial for Detection of Microbubble Acoustic Emissions

Following the ultrasonic transmission measurements, the optimized structure with 3 separate layers was investigated for detecting microbubble acoustic emissions in water. Encapsulated SonoVue microbubbles originally developed as ultrasound contrast agents for diagnostic imaging are responsive to ultrasound exposure, contracting and expanding during the positive and negative parts of the acoustic wave, respectively. They have been exploited in many acoustic cavitation-based therapeutic ultrasound studies[44] and were employed as the cavitation nuclei in the current study.

Figure 5a shows the experimental setup. A 1 inch planar immersion transducer (IDHF0.58R, NDT Systems Inc., CA, USA) was used as the transmitter to send the signals at the fundamental frequency toward the microbubbles. The Y-107 transducer was then used as the receiver both with and without the AMM in place. A waveform generator (33600A, Keysight Technologies, CA, USA) was programmed to send 25-cycle sine waves at 400 kHz, which were then amplified by an RF power amplifier (A150, Electronics & Innovation, Ltd., NY, USA) to drive the planar immersion transducer transmitting ultrasound pulses. This immersion transducer had a −6 dB bandwidth ranging from 350 to 600 kHz. Under water a silicone tube of 2 mm inner diameter and 1 mm wall thickness (Fisherbrand, Fisher Scientific UK. Ltd.) was placed perpendicular to the propagation of the ultrasound wave at a distance of 80 mm and in the far field of the transducer. The Y-107 transducer was cofocused with the transmitter at the tubing and aligned at 90° to both the tube and the transmitted filed. The relative position between the AMM and the Y-107 transducer was identical to that in numerical simulations.
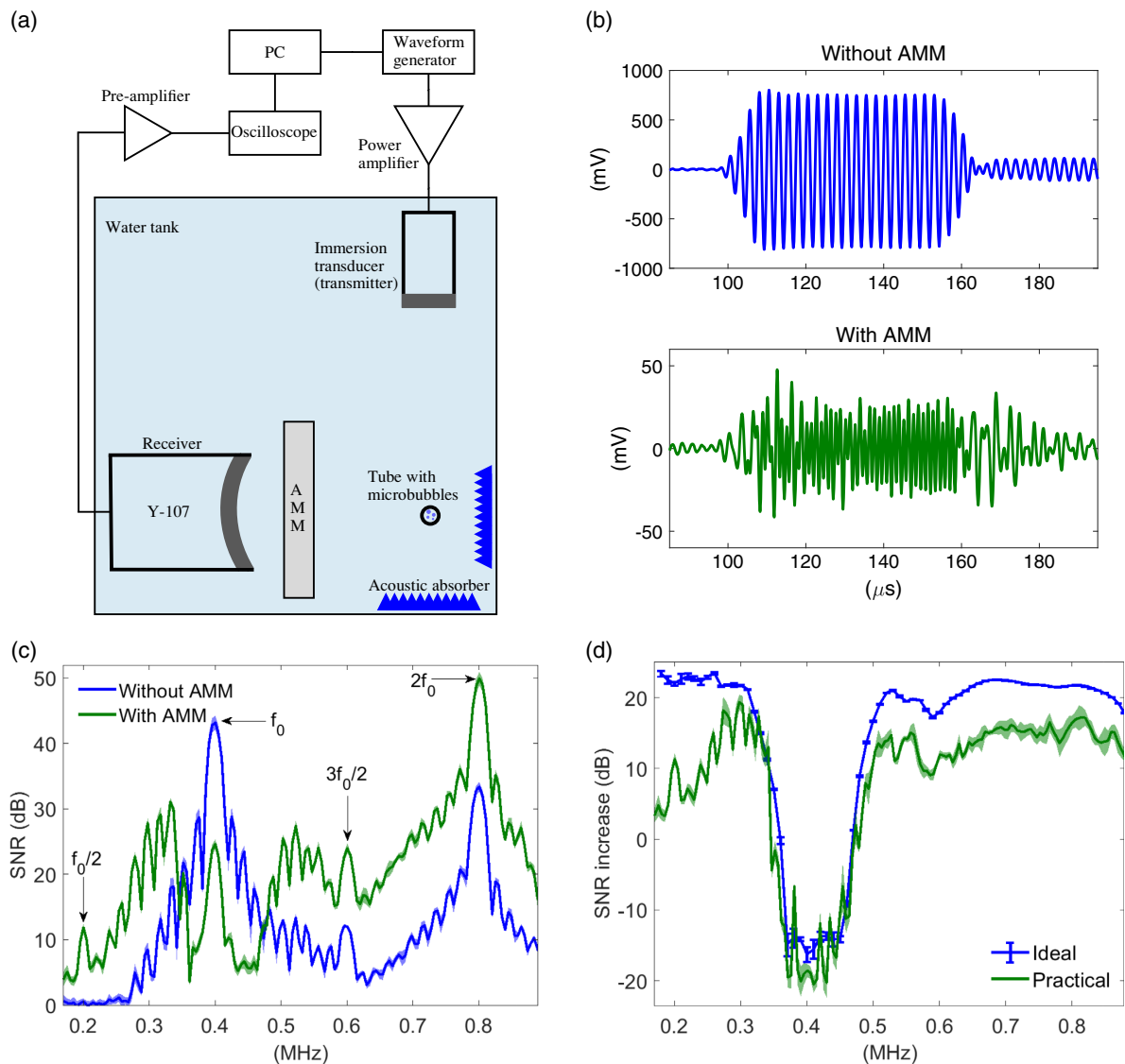
Figure 5. Measurement of microbubble acoustic emissions. a) Schematic diagram of the experimental setup. b) Typical oscilloscope recordings without (top) and with (bottom) the optimized AMM in place. c) Scattered acoustic spectra from microbubbles for the cases with and without the application of the optimized AMM. The standard deviation for each frequency was calculated from five repeats of the experiments. d) SNR improvement for the ideal data acquisition system and the practical microbubble experiment, when having the optimized AMM in place.

SonoVue microbubble solutions diluted by 1:1000 were injected into the tube, using a syringe driven by a pump (Aladdin AL-1000, World Precision Instruments) with a flow rate of $10 \, mL \, min^{-1}$. An average flow velocity of $53 \, mm \, s^{-1}$ was achieved in the tube. The microbubble populations were exposed to 25-cycle 400 kHz tone bursts with a peak negative pressure of 180 kPa measured by a 0.4 mm differential membrane hydrophone (Precision Acoustics, Dorchester, UK). The pressure was generated from the planar immersion transducer and the pressure measurement was carried out in a free field location without the AMM in place. A burst period of 0.7 s was used to allow the microbubbles to replenish the interrogation region between sonications. For each preparation of the microbubble solutions, 100 sonications were performed and in total five preparations were sonicated for statistical analysis. The acquired

signals were amplified by 30 dB with a preamplifier (5077PR, Olympus Industrial) and digitized by the MSO-S 104 A oscilloscope (used in Section 3.2) with a sampling frequency of 100 MHz. The oscilloscope recordings were downloaded to a local computer for subsequent analysis in MATLAB.

Typical recordings captured by the MSO-S 104A oscilloscope are given in Figure 5b. Without the AMM, a vertical scale of 250 mV/div was possible to avoid signal saturation. With the AMM placed in between the tube and the Y-107 detector, the fundamental component at 400 kHz was significantly attenuated. This allowed the harmonic signals to utilize more of the ADC dynamic range, with the vertical scale decreased to 15 mV/div on the oscilloscope. For both cases with and without the AMM in place, the reference waveform was captured, respectively, by flowing water through the tube with all other

parameters unchanged. Similarly, five repeats of 100 sonications were performed for each case. The mean of the 500 reference measurements was subtracted from the recordings with flowing microbubbles in the tube to remove the signals from the tubing and other mounts, and isolate the microbubble acoustic emissions.[45] In the frequency domain, each sequence of 100 measurements of microbubble acoustic emissions was averaged[46] with the error bar representing the standard deviation ($n = 5$) plotted for each frequency, as shown in Figure 5c. The reference of 0 dB in Figure 5c was the noise floor determined by averaging five repeats of 100 measurements without transmissions. The use of the optimized AMM increases the signal-to-noise ratio (SNR) of the detected harmonic emissions, with an average improvement of 11.8 and 11.9 dB for the subharmonic and ultraharmonic, respectively. In particular, the subharmonic component at 200 kHz, which is below the noise floor without using the AMM, can be clearly detected with the optimized AMM composed of 3 separate layers.

The corresponding SNR improvement could be estimated for an ideal data acquisition system without electronic noise and signal distortion. The SNR for an ideal N-bit ADC can be calculated by using

$$\mathrm{SNR}_{\mathrm{ideal}} = \log_2(R_{\mathrm{AD}} \times 2^N) \times 6.02 + 1.76\,\mathrm{dB},^{[19]}$$ where R_{AD} is the normalized ratio of the used ADC range. In the current study, the ideal SNR improvement could be calculated by

$$\begin{aligned}\Delta SNR_{\mathrm{ideal}} &= [\log_2(R_{\mathrm{ADAMM}} \times 2^N) - \log_2(R_{\mathrm{ADNoAMM}} \times 2^N)] \\ &\quad \times 6.02 + T(f) = \log_2(R_{\mathrm{ADAMM}}/R_{\mathrm{ADNoAMM}}) \\ &\quad \times 6.02 + T(f)\end{aligned}$$

where R_{ADAMM} and R_{ADNoAMM} are the normalized ratios of the ADC range used for the cases with and without the AMM, and $T(f)$ is the AMM transmission spectrum as a function of frequency f. By substituting $R_{\mathrm{ADAMM}}/R_{\mathrm{ADNoAMM}}$ with 250/15 (see Section 3.3) and $T(f)$ with the measured curve in Figure 4c, Figure 5d shows the estimation of the ideal SNR improvement compared with the practical values in monitoring microbubble acoustic emissions. These practical values were determined by subtracting the SNR curve without the AMM from that with the AMM (Figure 5c). Additional electronic noise and distortion processes in the practical data acquisition system[19] could account for the differences between the two curves beyond 240 kHz in Figure 5d. As plotted in Figure 5c, a clear separation between the signal and noise is impossible below 240 kHz, when the AMM was not in place. In this case, the overestimation of the SNR likely occurred for the frequencies lower than 240 kHz, resulting in the underestimation of the SNR improvement in Figure 5d. Overall, the transfer properties of the AMM can be reliably determined, and the practical SNR improvement due to the use of the AMM could vary with the data acquisition system and its configurations.

4. Discussion

Passive detection of microbubble emissions with high specificity is crucial to correctly uncover features of acoustic cavitation. The emissions at the fundamental and integer harmonics of the drive frequency are rarely used as metrics of acoustic cavitation, as both microbubbles and tissue scatter at those frequencies, making it difficult to have a clear separation between the signals generated from these two sources.[7] In contrast, the subharmonic and ultraharmonic nonlinearity are exclusive to microbubbles, making them useful indicators of acoustic cavitation. They set in when the driving pressure exceeds a threshold. The detection of the onset of these weak microbubble signatures provides a means for online optimization of the transmit parameters in cavitation-based ultrasound therapy.[13,14] The potential problem of this method arises from the fact that the minimum level of the detectable subharmonic or ultraharmonic signals is affected by the sensitivity of the measurement system as illustrated in Figure 5c. Techniques capable of improving the detection of weak microbubble harmonic signals are thus highly desirable for more accurate monitoring of the cavitation activity. By selectively removing the fundamental frequency component with the optimized AMM placed in water, the resultant harmonic emissions utilized more of the ADC dynamic range, being less affected by quantization errors.[19] Being a purely mechanical device, there are no issues with extra noise that could be added by analog electronic filters consisting of circuit components, potentially providing a better SNR. The combination of magnetic resonance imaging (MRI) and cavitation monitoring is desired especially in transcranial ultrasound therapy,[47,48] but designing an MRI-compatible band-stop filter is not trivial.[49] On the other hand, the AMMs made of titanium could provide another route for MRI-compatible filtering in the equipment bore.

The subharmonic of the drive frequency has a range of applications apart from the use for indicating the occurrence of acoustic cavitation. For example, it has been used to calculate the stable cavitation dose, by integrating the signal power in the frequency domain.[50] In addition, the subharmonic energy spectrum density has been investigated to correlate with blood–brain barrier permeability, constituting a potential indicator of treatment outcome.[15] Both stable and inertial cavitation find their utility in therapeutic ultrasound.[11] The broadband noise emissions (above 1 MHz) associated with inertial cavitation will not be efficiently measured with the AMM placed in front of the receiver, as frequency ranges with low transmission were found above 1 MHz through numerical simulations. But it is possible to reliably detect the presence of inertial cavitation by analyzing the microbubble emission spectra within a limited bandwidth around the subharmonic peak (e.g., 200–400 kHz for a drive frequency of 612 kHz[51]). Note also that there have been studies investigating the use of subharmonic emissions for quantification of inertial cavitation.[52,53] The proposed AMM could thus improve monitoring of both cavitation regimes in ultrasound therapy by using the detected subharmonic emissions with high sensitivity.

Additive manufacturing provides a flexible way to create 3D bandgap AMMs of complex geometries for operation in water, which is impossible by using conventional manufacturing methods. The coupling of waves from both water (longitudinal waves) and the inclusions of metal (shear waves) was found to significantly affect the transmission spectrum. This is different from the cases in air,[32,40,54] where ultrasound waves only propagate through the solid inclusions, with the AMM tightly sandwiched between the transmitter and receiver. For a realistic design, the

water coupling was used between a set of separate 3D layers to stop the propagation of shear waves. The properties of the spectral bandgaps can be tuned by different means. While keeping the materials and the lattice structure constant, the width and position of the bandgap can be altered by modifying the geometric parameters as shown in Figure 2a,b. The change of the constituent material also affects the bandgap formation as illustrated in **Figure 6**. For the optimized design, the use of an inclusion material with a higher acoustic impedance contrast to the transmission medium of water could shift the bandgap to higher frequencies.

The effects of the struts linking adjacent 3D layers were investigated in Section 2. The performance of a single 3D layer was found to be fundamental in determining the capability of the final AMM multilayer structure. The struts comprising the unit cell might also play a role in changing the transfer properties of a single layer. The effects when having different arrangements of struts in each unit cell were then investigated by using numerical simulations with a single 3D layer. The identical parameters used for Figure 2c were adopted. For a realizable design, the struts cannot be totally removed, and at least the ones along either the y or z axis (see Figure 1b) are needed to hold the whole structure together. The unit cells were arranged symmetrically about the x axis, and thus the effects of struts along the y and z axes were interchangeable, simplifying the simulations. The results are shown in **Figure 7**, and the influence when having the struts along the x axis is noticeable, where the attenuation is much higher within the bandgap. Within a single 3D layer, the propagation of shear waves along the x-direction struts was found to account for this beneficial phenomenon, while it became a detrimental factor when having multiple continuous (i.e., interconnected) layers as demonstrated in Section 2, and a separate-layer design was thus proposed. As shown in Figure 7, the location of the bandgap can be shifted by using struts orientated along different axes. Thus, the struts comprising the unit cell play an important role in determining the AMM transfer properties. Note that, in practice, struts have to be present in order to hold the whole structure together.
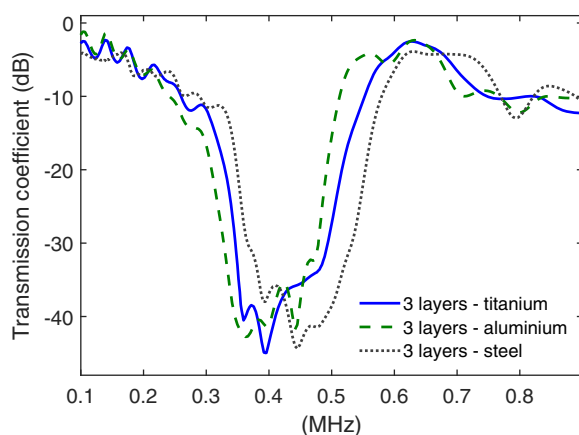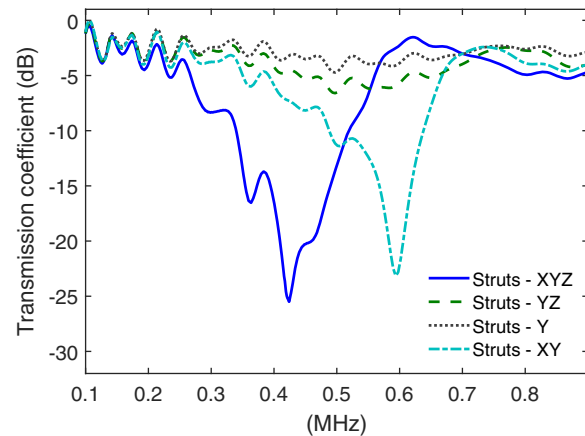
Figure 7. Numerical simulations of bandgap properties for a single 3D layer with different strut orientations in each unit cell. Identical parameters as those reported in Figure 2c were used ($a = 1.4$ mm, $R = 0.25a$, and $r = 0.16a$).

Numerical simulations were used to study the effect of the AMM lateral position on its transfer properties by moving the 3-separate-layer AMM along the x axis (see Figure 1) with steps of 2.5 mm. In **Figure 8**a, the response is shown at various positions (X Bias) relative to that shown earlier in Section 2. It was found that, at normal incidence where the main axis of propagation was normal to the sample surface, the position of the AMM along the x axis had only a small effect on the transfer properties, and relatively stable bandgap and spectral pass bands were formed at the positions shown. Conversely, rotating the AMM face away from alignment with the x axis had a bigger effect. This is shown in Figure 8b, where the AMM was rotated in angle increments of 10°. The results indicate that, in general, the attenuation of signals across the bandgap frequency range decreases at larger angles, which is undesirable. Note also that the bandgap structure becomes less stable, with large variations in amplitude noted at 30°. This effect occurs because the phases of signals across the output side of the AMM would become asymmetrical due to refraction effects. This would then cause a deterioration in coherent summation at the receiver surface. Note that the AMM was designed for a particular direction of travel through the structure (at normal incidence) to obtain the desired bandgap, and a deviation from this would affect the bandgap properties.

In this study, the whole transmit/receive pair has been simulated to optimize an AMM, and the approach adopted could be extended to different applications involving other specific transmit/receive units. The attenuation level in the transmission spectrum can be controlled by using a different number of layers. In general, the greater the number of layers, the higher is the attenuation of signals. This also applies to frequencies outside the bandgap where the signal transmission levels will also be reduced with more layers. Thus, three layers were chosen as the best compromise so as to not only achieve the required bandgap but also to allow reasonable transmission levels at the passband frequencies. For a given structure, characterization by modeling is necessary to predict the corresponding filtering
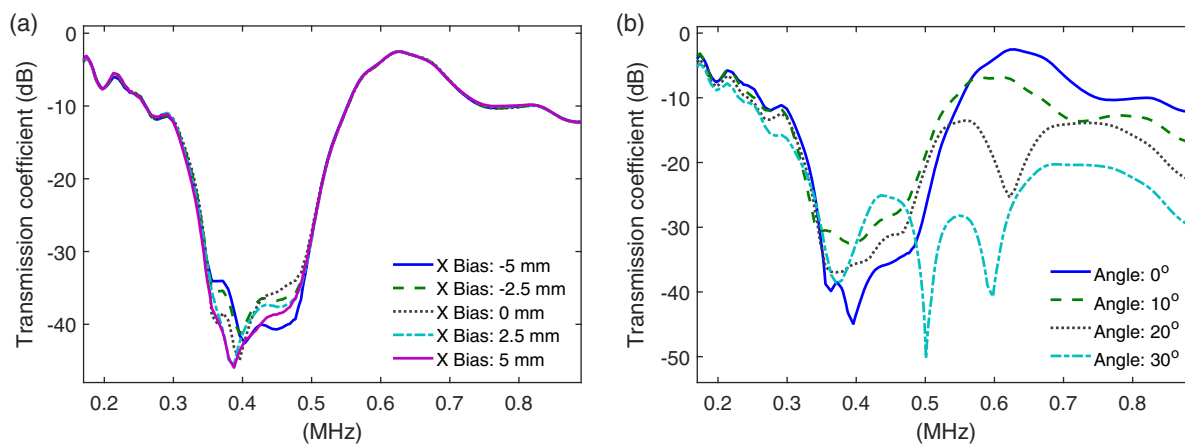

Figure 6. Numerical simulations: the effect of varying the inclusion material on bandgap properties. Identical parameters as used for the optimized AMM design were adopted for all three curves: 3 separate layers, $a = 1.4$ mm, $R = 0.25a$, and $r = 0.16a$.

Figure 8. Numerical simulations: a) the effect of the AMM position (along the *x* axis) on bandgap properties; b) the effect of changing the angle of incidence away from normal incidence (0°) to 30°. Identical AMM structural parameters to those given for Figure 2c were used (i.e., $a = 1.4$ mm, $R = 0.25a$, and $r = 0.16a$).

capability. In practice, the ultimate attenuation level in the bandgap would be limited by the accuracy of manufacturing, where manufacturing imperfections make the destructive interference that results in the bandgap incomplete. When this occurs, small-amplitude wave modes would exist within the bandgap even if more layers are employed, and zero transmission would then be difficult to achieve. A range of 3D unit cells have been proposed to create bandgaps prohibiting the propagation of acoustic waves along all directions. When immersed in water, the effect of shear waves on bandgap properties would need to be investigated for each design, as exemplified in Section 2. In addition, the structure has been designed for scalability. With advances in manufacturing scalability,[55] 3D topologies whose feature size spans from tens of nanometers to tens of centimeters can be printable. It is important to understand the resolution limit of an available additive manufacturing approach and the tolerance of manufacturing imperfections to avoid undermining the metamaterial properties significantly. The applicability of the design to different regions of frequencies could be extended provided the lattice constant can be scaled accordingly. To simultaneously open multiple bandgaps at different frequencies, the method of stacking AMMs of different designs could be explored.[56]

5. Conclusion

In conclusion, we propose using an AMM for suppressing unwanted ultrasound signals when they propagate in water, which requires no modification to the electronic hardware components and significantly improves the detection sensitivity of microbubble emissions. This is the first time that AMMs have been applied to passive acoustic monitoring, and AMMs stand to improve treatment outcomes during acoustic cavitation-based ultrasound treatments. For operation in water, the remarkable effect of shear waves on AMM transfer properties has been highlighted. An optimized design capable of providing stable bandgaps with increased sample thickness has been presented, being achieved by cutting off shear wave propagation through adjacent layers, with water gaps placed in between. To be adaptable to different applications, the bandgap properties can be

tuned via different ways. With the continuous development of additive manufacturing approaches with finer-scale control, more complex and effective bandgap metamaterials could be conceived and fabricated.

Conflict of Interest

The authors declare no conflict of interest.

Data Availability Statement

The data that support the findings of this study are available from the corresponding author upon reasonable request.

[1] J.-M. Escoffre, A. Bouakaz, *Therapeutic Ultrasound*, Vol. *880*, Springer, Berlin **2015**.
[2] G. Ter Haar, C. Coussios, *Int. J. Hyperthermia* **2007**, *23*, 89.

[3] C. Poon, D. McMahon, K. Hynynen, *Neuropharmacology* **2017**, *120*, 20.

[4] J. J. Choi, K. Selert, F. Vlachos, A. Wong, E. E. Konofagou, *Proc. Natl. Acad. Sci.* **2011**, *108*, 16539.

[5] C. Zhang, C. Liu, W. He, D. Jiao, Z. Liu, *Appl. Mater. Today* **2021**, *22*, 100897.

[6] O. Vince, S. Peeters, V. A. Johanssen, M. Gray, S. Smart, N. R. Sibson, E. Stride, *Adv. Healthcare Mater.* **2021**, *10*, 2001343.

[7] J. McLaughlan, I. Rivens, T. Leighton, G. Ter Haar, *Ultrasound Med. Biol.* **2010**, *36*, 1327.

[8] C. Mannaris, B. M. Teo, A. Seth, L. Bau, C. Coussios, E. Stride, *Adv. Healthcare Mater.* **2018**, *7*, 1800184.

[9] M. I. Gutierrez, E. H. Penilla, L. Leija, A. Vera, J. E. Garay, G. Aguilar, *Adv. Healthcare Mater.* **2017**, *6*, 1700214.

[10] K. Kooiman, S. Roovers, S. A. Langeveld, R. T. Kleven, H. Dewitte, M. A. O'Reilly, J.-M. Escoffre, A. Bouakaz, M. D. Verweij, K. Hynynen, I. Lentacker, E. Stride, C. K. Holland, *Ultrasound Med. Biol.* **2020**, *46*, 1296.

[11] A. N. Thomas, E. Stride, *J. Nuffield Department Surg. Sci.* **2020**, *1*, 3.

[12] N. McDannold, N. Vykhodtseva, K. Hynynen, *Phys. Med. Biol.* **2006**, *51*, 793.

[13] M. A. O'Reilly, K. Hynynen, *Radiology* **2012**, *263*, 96.

[14] A. Burgess, S. Dubey, S. Yeung, O. Hough, N. Eterman, I. Aubert, K. Hynynen, *Radiology* **2014**, *273*, 736.

[15] C.-H. Tsai, J.-W. Zhang, Y.-Y. Liao, H.-L. Liu, *Phys. Med. Biol.* **2016**, *61*, 2926.

[16] M. A. O'Reilly, R. M. Jones, K. Hynynen, *IEEE Trans. Biomed. Eng.* **2014**, *61*, 1285.

[17] T. Sun, Y. Zhang, C. Power, P. M. Alexander, J. T. Sutton, M. Aryal, N. Vykhodtseva, E. L. Miller, N. J. McDannold, *Proc. Natl. Acad. Sci.* **2017**, *114*, E10281.

[18] K. Johansen, J. H. Song, P. Prentice, *Ultrason. Sonochem.* **2018**, *43*, 146.

[19] K. H. Lundberg, Ph.D. thesis, *Massachusetts Institute of Technology*, **2002**.

[20] J. R. McLaughlan, Ph.D. thesis, Institute of Cancer Research (University of London), **2008**.

[21] M. Zhou, S. Ouzounov, M. Mischi, E. Cantatore, P. Harpe, in *2019 IEEE Int. Ultrasonics Symp. (IUS)*, IEEE, Piscataway, NJ **2019**, pp. 993–996.

[22] M.-H. Lu, L. Feng, Y.-F. Chen, *Mater. Today* **2009**, *12*, 34.

[23] S. A. Cummer, J. Christensen, A. Alù, *Nat. Rev. Mater.* **2016**, *1*, 1.

[24] P. A. Deymier, Acoustic Metamaterials and Phononic Crystals, Vol. *173*, Springer Science & Business Media, Berlin **2013**.

[25] G. Liao, C. Luan, Z. Wang, J. Liu, X. Yao, J. Fu, *Adv. Mater. Technol.* **2021**, *6*, 2000787.

[26] H. Zhu, F. Semperlotti, *AIP Adv.* **2013**, *3*, 092121.

[27] A. Khelif, B. Djafari-Rouhani, J. Vasseur, P. Deymier, *Phys. Rev. B* **2003**, *68*, 024302.

[28] C. Croënne, E. Lee, H. Hu, J. Page, *AIP Adv.* **2011**, *1*, 041401.

[29] Z. Liu, X. Zhang, Y. Mao, Y. Zhu, Z. Yang, C. T. Chan, P. Sheng, *Science* **2000**, *289*, 1734.

[30] Y. Chen, H. Yao, L. Wang, *J. Appl. Phys.* **2013**, *114*, 043521.

[31] L. D'Alessandro, E. Belloni, R. Ardito, A. Corigliano, F. Braghin, *Appl. Phys. Lett.* **2016**, *109*, 221907.

[32] F. Lucklum, M. J. Vellekoop, *Appl. Phys. Lett.* **2018**, *113*, 201902.

[33] A. Konstantopoulou, N. Aravantinos-Zafiris, M. Sigalas, *J. Appl. Phys.* **2020**, *127*, 075101.

[34] M. Askari, D. A. Hutchins, P. J. Thomas, L. Astolfi, R. L. Watson, M. Abdi, M. Ricci, S. Laureti, L. Nie, S. Freear, R. Wildman, C. Tuck, M. Clarke, E. Woods, A. T. Clare, *Addit. Manuf.* **2020**, *36*, 101562.

[35] M. Askari, D. A. Hutchins, R. L. Watson, L. Astolfi, L. Nie, S. Freear, P. J. Thomas, S. Laureti, M. Ricci, M. Clark, A. T. Clare, *Addit. Manuf.* **2020**, *35*, 101309.

[36] E. Dogan, A. Bhusal, B. Cecen, A. K. Miri, *Appl. Mater. Today* **2020**, *20*, 100752.

[37] P. R. Hoskins, K. Martin, A. Thrush, Diagnostic Ultrasound: Physics and Equipment, CRC Press, Boca Raton **2019**.

[38] S. Laureti, D. A. Hutchins, L. Astolfi, R. L. Watson, P. J. Thomas, P. Burrascano, L. Nie, S. Freear, M. Askari, A. T. Clare, M. Ricci, *Sci. Rep.* **2020**, *10*, 1.

[39] J. A. Jensen, S. I. Nikolov, K. L. Gammelmark, M. H. Pedersen, *Ultrasonics* **2006**, *44*, 5.

[40] F. Lucklum, M. J. Vellekoop, in 2016 IEEE Int. Ultrasonics Symp. (IUS), IEEE, Piscataway, NJ **2016**, pp. 1–4.

[41] A. Khelif, F.-L. Hsiao, A. Choujaa, S. Benchabane, V. Laude, *IEEE Trans. Ultrason. Ferroelectr. Freq. Control* **2010**, *57*, 1621.

[42] D. Herzog, V. Seyda, E. Wycisk, C. Emmelmann, *Acta Mater.* **2016**, *117*, 371.

[43] J. D. Achenbach, Reciprocity In Acoustics, 55–69, Cambridge Monographs On Mechanics. Cambridge University Press, Cambridge **2004**.

[44] A. Dauba, A. Delalande, H. A. Kamimura, A. Conti, B. Larrat, N. Tsapis, A. Novell, *Pharmaceutics* **2020**, *12*, 1125.

[45] M. A. O'Reilly, K. Hynynen, *IEEE Trans. Biomed. Eng.* **2010**, *57*, 2286.

[46] J. R. McLaughlan, S. Harput, R. H. Abou-Saleh, S. A. Peyman, S. Evans, S. Freear, *Ultrasound Med. Biol.* **2017**, *43*, 346.

[47] R. M. Jones, K. Hynynen, *Br. J. Radiol.* **2019**, *92*, 20180601.

[48] N. Lipsman, Y. Meng, A. J. Bethune, Y. Huang, B. Lam, M. Masellis, N. Herrmann, C. Heyn, I. Aubert, A. Boutet, G. S. Smith, K. Hynynen, S. E. Black, *Nat. Commun.* **2018**, *9*, 1.

[49] R. A. Stevenson, G. A. Kustra, *US Patent 8,788,057 B2* **2014**.

[50] S.-K. Wu, P.-C. Chu, W.-Y. Chai, S.-T. Kang, C.-H. Tsai, C.-H. Fan, C.-K. Yeh, H.-L. Liu, *Sci. Rep.* **2017**, *7*, 1.

[51] R. M. Jones, D. McMahon, K. Hynynen, *Theranostics* **2020**, *10*, 7211.

[52] H. Hasanzadeh, M. Mokhtari-Dizaji, S. Z. Bathaie, Z. M. Hassan, *Ultrason. Sonochem.* **2010**, *17*, 863.

[53] H. Hasanzadeh, M. Mokhtari-Dizaji, S. Z. Bathaie, Z. M. Hassan, V. Nilchiani, H. Goudarzi, *Ultrason. Sonochem.* **2011**, *18*, 394.

[54] F. Lucklum, M. J. Vellekoop, *IEEE Trans. Ultrason. Ferroelectr. Freq. Control* **2016**, *63*, 796.

[55] X. Zheng, W. Smith, J. Jackson, B. Moran, H. Cui, D. Chen, J. Ye, N. Fang, N. Rodriguez, T. Weisgraber, C. M. Spadaccini, *Nat. Mater.* **2016**, *15*, 1100.

[56] M. Shen, W. Cao, *Appl. Phys. Lett.* **1999**, *75*, 3713.